Journal of Physics:
Condensed Matter

PAPER • **OPEN ACCESS**

Parameterizing empirical interatomic potentials for predicting thermophysical properties via an irreducible derivative approach: the case of ThO_2 and UO_2

To cite this article: Shuxiang Zhou *et al* 2025 *J. Phys.: Condens. Matter* **37** 255901

OPEN ACCESS
IOP Publishing
Journal of Physics: Condensed Matter
J. Phys.: Condens. Matter **37** (2025) 255901 (8pp)
https://doi.org/10.1088/1361-648X/ade10a

Parameterizing empirical interatomic potentials for predicting thermophysical properties via an irreducible derivative approach: the case of ThO_2 and UO_2

Shuxiang Zhou[1,*], Chao Jiang[1], Enda Xiao[2], Sasaank Bandi[3], Michael W D Cooper[4], Miaomiao Jin[5], David H Hurley[1], Marat Khafizov[6] and Chris A Marianetti[3]

[1] Idaho National Laboratory, Idaho Falls, ID 83415, United States of America
[2] Department of Chemistry, Columbia University, New York, NY 10027, United States of America
[3] Department of Applied Physics and Applied Mathematics, Columbia University, New York, NY 10027, United States of America
[4] Los Alamos National Laboratory, Los Alamos, NM 87545, United States of America
[5] Department of Nuclear Engineering, The Pennsylvania State University, University Park, PA 16802, United States of America
[6] Department of Mechanical and Aerospace Engineering, The Ohio State University, Columbus, OH 43210, United States of America

E-mail: shuxiang.zhou@inl.gov

Received 2 April 2025, revised 8 May 2025
Accepted for publication 4 June 2025
Published 13 June 2025

Abstract

The accuracy of classical physical property predictions using molecular dynamics simulations is determined by the quality of the interatomic potentials. Here we introduce a training approach for empirical interatomic potentials (EIPs) which is well suited for capturing phonons and phonon-related properties. Our approach is based on direct comparisons of the second- and third-order irreducible derivatives (IDs) between an EIP and the Born–Oppenheimer potential within density functional theory (DFT) calculations. IDs fully exploit space group symmetry and allow for training without redundant information. We demonstrate the fidelity of our approach in the context of ThO_2 and UO_2, where we optimize parameters of an embedded-atom method potential in addition to core–shell interactions. Our EIPs provide thermophysical properties in good agreement with DFT and outperform widely utilized EIPs for phonon dispersion and thermal conductivity predictions. Reasonable estimates of thermal expansion and formation energies of Frenkel pairs are also obtained.

* Author to whom any correspondence should be addressed.

Supplementary material for this article is available online

Keywords: empirical potential, nuclear fuel, density functional theory, phonon, phonon transport

1. Introduction

Interatomic potentials are mathematical models used to encode the Born–Oppenheimer potential of some collection of atoms. Traditionally, empirical interatomic potentials (EIPs) are derived using analytical functional forms with a few parameters: examples include the Lennard–Jones potential [1], which has only two parameters in simple systems, and the Tersoff potential [2] and embedded atom method (EAM) potential [3], which both have tens of parameters. The analytical functional forms and the limited number of parameters of EIPs offer simplicity for modeling, but also restrict accuracy and limit the potential for capturing complex phenomena. Recently, machine-learning interatomic potentials (MLIPs) have emerged as a valuable complement to traditional EIPs by leveraging machine-learning algorithms like neural networks and Gaussian process regression [4, 5], exhibiting higher accuracy and transferability. However, MLIPs are computationally more demanding, often using thousands to millions of parameters. Despite the success of MLIPs, EIPs are still useful given their computational efficiency and physical interpretability.

In the last few decades, extensive studies have been performed to advance the training procedure for interatomic potentials. EIPs were previously trained by fitting to experimental measurements, including the lattice parameters, elastic constants, thermal expansion, and specific heat [2, 3, 6, 7]. As training data, experimental measurements are limited by both quantity and quality. In terms of quantity, experiments are often limited by high-cost and time-consuming processes, especially for complex systems such as defect structures. Additionally, experiments are limited in terms of directly probing the details of the Born–Oppenheimer potential, and instead only measure averaged quantities. This lack of data can limit the accuracy of the EIP and can yield substantial errors for selected observables. For example, traditional parametrization of EIPs to elastic constants and thermal expansion is often inadequate for accurately predicting phonon dispersions, not to mention third-order phonon interactions [8]. Both the challenge of quantity and quality of training data can be resolved by utilizing first-principles calculations, where approaches such as density functional theory (DFT) can produce a multitude of atomistic data at both equilibrium and non-equilibrium.

Given that the goal of parameterizing an interatomic potential is to faithfully encode the Born–Oppenheimer potential, a natural source of training data would be a direct sampling of the Born–Oppenheimer potential over some relevant domain, which can be achieved when using data from sufficiently reliable first-principles calculations. There are various approaches for sampling the Born–Oppenheimer potential. One approach would be to compute the value of the Born–Oppenheimer potential (i.e. energy) and the first derivatives (i.e. forces) at a collection of configurations, which is practical for approaches such as DFT where the forces can be computed at a small computational overhead. The collection of configurations might be generated using a molecular dynamics (MD) trajectory. EIPs trained on DFT-calculated energies and forces have generated robust results, including reasonable predictions of phonons [9–15] and defect energies [16]. It is standard to train MLIPs on DFT-calculated forces and energies [17], which has yielded robust MLIPs in a broad range of systems [17], including molten salt systems [18, 19]. An alternative approach would be to use a single minimum energy configuration and construct the second and third derivatives of the Born–Oppenheimer potential of this configuration. The use of second- and higher-order derivatives in potential training is relatively uncommon compared to the utilization of energies and forces, both due to the increased computational cost of generating the data and training the model. However, if the targeted observables to be generated using the EIP directly probe the derivatives (e.g. scattering function), using the second and higher order derivatives as training data may be worthwhile. For example, interatomic potentials trained using DFT-calculated second energy derivatives can significantly improve the predicted phonon dispersion, for both EIP [20–25] and MLIP [26, 27]. When training to second- and higher-order energy derivatives, it is important not to have any redundancy in the training data, which can be achieved using space group irreducible derivatives (IDs) [28]. The IDs are generated using the group theoretical selection rules which dictate which irreducible representations are allowed to couple, providing a minimal set of derivatives that characterize a given discretization of the Brillouin zone. Therefore, when training an EIP or an MLIP to derivatives of the Born–Oppenheimer potential, using IDs as training data will clearly offer improvements.

In this work, we develop an ID-based potential training approach by including the second- and third-order displacement IDs and the second-order strain IDs in the training data. This approach is used to parameterize an EIP for the nuclear fuel materials ThO_2 and UO_2, as there is a critical need to understand defect formation, microstructure evolution, and thermal transport degradation [29]. For actinide oxides, a previously developed EIP [7], referred to as the CRG potential, has found widespread use in classical MD studies [30–32]. The CRG potential was parameterized in a traditional fashion, based on the experimental elastic constant and thermal expansion. Recently, the accuracy of the CRG potential for predicting phonons and thermal transport within the Boltzmann transport equation (BTE) framework was assessed, demonstrating that the CRG potential has nontrivial differences with

the experimental phonon dispersion of optical branches as well as with the thermal conductivity [33]. These differences are not unexpected, given that neither the phonons nor the phonon interactions were included in the CRG training data. In this work, we demonstrate that our ID-based training procedure yields an EIP that reliably characterizes the first-principles data. Given that DFT and DFT+U can reliably describe ThO_2 and UO_2 [34–36], respectively, our resulting EIP yields a substantial improvement over the CRG potential for the predicted phonon-related properties relative to experiment.

2. Methods

2.1. Potential form

In this work, the analytical expression of the EIP is based on the CRG potential [7], which uses a pair-potential for each atom pair in addition to the many-body EAM potential [3]. The pair-potential contains three contributions: the Buckingham potential [37], the Morse potential [38], and the long-range electrostatic Coulomb interaction. Additionally, a core–shell spring model [39] is added, as it substantially improves the prediction of selected optical phonons in UO_2 [40, 41]. Within the core–shell model, each ion splits into two particles, a core and a shell, where the core and shell are attached by a spring force with spring constant k (see the last term of equation (1)). The charge and mass of the ion also split into a core and shell contribution, and here we apply the massless shell model, as implemented in the general utility lattice program (GULP) package [42]. The non-Coulombic interactions (i.e. Buckingham potential, Morse potential, and EAM) are only defined between the shells, while Coulombic interactions are applied between all cores and shells, except the core and shell of the same ion [39] (see equation (3)).

We denote the distances between the core–shell ion i and j as a vector $\mathbf{r_{ij}} = (r_{ij}^{cc}, r_{ij}^{cs}, r_{ij}^{sc}, r_{ij}^{ss})$, where r_{ij}^{cc}, r_{ij}^{cs}, r_{ij}^{sc}, r_{ij}^{ss} represent the distance between i's core and j's core, i's core and j's shell, i's shell and j's core, and i's shell and j's shell, respectively. The potential energy E_i of an ion i concerning all other ions is given by:

$$E_i = \frac{1}{2}\sum_{j\neq i}\phi_{\alpha\beta}\left(\mathbf{r_{ij}}\right) - G_\alpha\sqrt{\sum_{j\neq i}\sigma_\beta\left(r_{ij}^{ss}\right)} + \frac{1}{2}k_i r_{ii}^{cs\,2}, \quad (1)$$

which is a sum of pairwise components, many-body components, and harmonic spring component terms. The pairwise potential between ions i and j, $\phi_{\alpha\beta}(\mathbf{r_{ij}})$, is given by the sum of the Coulomb potential $\phi_C(\mathbf{r_{ij}})$, the Buckingham potential $\phi_B(r_{ij}^{ss})$, and the Morse potential $\phi_M(r_{ij}^{ss})$:

$$\phi_{\alpha\beta}\left(\mathbf{r_{ij}}\right) = \phi_C\left(\mathbf{r_{ij}}\right) + \phi_B\left(r_{ij}^{ss}\right) + \phi_M\left(r_{ij}^{ss}\right), \quad (2)$$

$$\phi_C\left(\mathbf{r_{ij}}\right) = \frac{1}{4\pi\epsilon_0}\left(\frac{q_\alpha^c q_\beta^c}{r_{ij}^{cc}} + \frac{q_\alpha^c q_\beta^s}{r_{ij}^{cs}} + \frac{q_\alpha^s q_\beta^c}{r_{ij}^{sc}} + \frac{q_\alpha^s q_\beta^s}{r_{ij}^{ss}}\right), \quad (3)$$

$$\phi_B\left(r_{ij}^{ss}\right) = A_{\alpha\beta}\exp\left(\frac{-r_{ij}^{ss}}{\rho_{\alpha\beta}}\right) - \frac{C_{\alpha\beta}}{\left(r_{ij}^{ss}\right)^6}, \quad (4)$$

$$\phi_M\left(r_{ij}^{ss}\right) = D_{\alpha\beta}\left[\mathrm{e}^{-2\gamma_{\alpha\beta}\left(r_{ij}^{ss}-r_0\right)} - 2\mathrm{e}^{-\gamma_{\alpha\beta}\left(r_{ij}^{ss}-r_0\right)}\right], \quad (5)$$

where α and β are the labels of species for ions i and j, respectively. The many-body term in equation (1) is given by the square root of the sum of the pairwise function $\sigma_\beta(r_{ij}^{ss})$, given by:

$$\sigma_\beta\left(r_{ij}^{ss}\right) = \frac{n_\beta}{r_{ij}^{ss\,8}}. \quad (6)$$

2.2. Training procedure and model assessment

Due to the specific interests in phonon predictions, our dataset was separated into two categories: phonon-related properties and other properties. Phonon-related properties contain the second-order displacement IDs, the third-order displacement IDs, the second-order strain IDs, and phonon thermal conductivity. Besides these phonon-related properties, we consider the classical lattice parameter $a(T)$ at $T = 0$ K, the normalized Born effective charges Z_α^*, and the defect formation energy (E_F) of Frenkel pairs (FPs). Here Z_α^* is obtained by the Born effective charge Z_α normalized by the dielectric constant ϵ: $Z_\alpha^* = Z_\alpha/\sqrt{\epsilon}$. Among the different types of point defects, only the FP is considered, so a direct comparison can be made between DFT and the EIP, avoiding approximations needed to treat unbalanced charges. The training dataset contained the second-order displacement IDs within the $2\times2\times2$ supercell, the third-order displacement IDs within the conventional cubic supercell $\hat{\mathbf{S}}_\mathrm{C}$, the second-order strain IDs, $a(0)$, Z_α^*, and E_F for a Th or U FP in the conventional cubic supercell, while the remaining data were used to assess the accuracy of the model. The details of properties used in the training procedure and assessment are tabulated in table S1 of the supplemental materials (SM) [43]. Additionally, we also predicted thermal expansion using the EIP and directly compared it with experimental results. See section I of SM [43] for the mathematical representation of the supercells used in calculations, following reference [28].

All DFT calculations were carried out via a projector augmented-wave (PAW) method [44, 45], as implemented in the Vienna *ab initio* simulation package [46, 47]. For the exchange-correlation functionals, the strongly constrained and appropriately normed (SCAN) [48] functional was used for ThO_2, while the Perdew, Burke, Ernzerhof (PBE) generalized gradient approximation (GGA) [49] was used for UO_2, following previous DFT studies [34–36, 50–52] which yield phonons in good agreement with experiments. Additionally, the UO_2 calculations applied spin–orbit coupling, DFT+U [53, 54] with $U = 4$ eV, and occupation matrix control with the initial values of the occupation matrices from the 3**k** AFM state reported in [35]. The plane-wave cutoff energy was set to 550 eV, and the energy convergence criterion was set to 10^{-6} eV. For the primitive cell, a Γ-centered $13\times13\times13$ k-point mesh [55] was applied; for supercells, the k-point densities were kept approximately the same. The second-order displacement IDs and the second-order strain IDs were calculated using the lone ID approach, and

Table 1. Parameters for the short-range pairwise potentials described by equations (4) and (5).

Interaction	$\phi_B(r_{ij})$			$\phi_M(r_{ij})$		
α-β	$A_{\alpha\beta}$ (eV)	$\rho_{\alpha\beta}$ (Å)	$C_{\alpha\beta}$ (eV Å^6)	$D_{\alpha\beta}$ (eV)	$\gamma_{\alpha\beta}$ (Å^{-1})	r_0 (Å)
Th-Th	16 078.23	0.2985	1.6499	5.0866	5.7739	2.4611
U-U	18 447.13	0.1452	12.9937	6.2571	4.2394	2.1289
Th-O	859.98	0.3820	9.7412	0.3241	2.1530	2.4440
U-O	807.24	0.3895	6.0011	0.3088	1.9770	2.5195
O-O	958.50	0.3202	7.0602	—	—	—

Table 2. Parameters for the many-body term, the Coulomb potential, and core–shell models described by equations (1), (3), and (6).

Species	G_α (eV Å$^{1.5}$)	n_α (Å^5)	q^c_α ($\|e\|$)	q^s_α ($\|e\|$)	k_α (eV Å^{-2})
Th	1.1122	899.84	−9.7268	12.6813	1204.99
U	2.0053	991.90	−7.2900	10.2445	551.98
O	0.4772	986.88	1.7688	−3.2461	436.86

the third-order displacement IDs were calculated using the bundled ID approach [28]. All second-order displacement IDs (phonon dispersion) commensurate with the $4 \times 4 \times 4$ supercell were computed, while all third-order displacement IDs commensurate with the non-diagonal supercell $\hat{\mathbf{S}}_{\mathrm{O}}$ were computed. The thermal conductivity is computed within the relaxation time approximation (RTA) using a $12 \times 12 \times 12$ **q**-mesh. The formation energy E_F of FPs is computed with the volume fixed, while the interstitial is located in the octahedral site.

The GULP package [42] was applied to calculate the static properties of EIPs, including lattice parameter, force, energy, dielectric constant, and Born effective charge. The Coulomb interactions were implemented using the Ewald summation [56], where an 11.0 Å cut-off was applied for both the pairwise and many-body interactions. For thermal expansion, MD simulations were performed by GULP in an NPT ensemble at T up to 3000 K using the non-diagonal supercell $4\hat{\mathbf{S}}_{\mathrm{C}}$. Each MD simulation runs 5 ps with a time step of 2 fs, while $a(T)$ is obtained by averaging the last 4 ps.

The parameter optimization for the EIPs was carried out using the potential Pro-Fit package [57], which minimizes the total error e, given by:

$$e = \sqrt{\sum (w_i e_i)^2}, \tag{7}$$

where w_i and e_i are the weight and error, respectively, for the ith training data. The parameter optimization method was provided as a flowchart in section II of SM [43], and the weight of training data is tabulated in table S1 of SM [43]. Throughout this work, we denote our trained EIP as the present work (PW), and its optimized parameter values are presented in tables 1 and 2. To demonstrate the robustness of our training method, two alternative potential forms without the core–shell model have also been trained, and improvements of thermophysical predictions relative to the CRG potential are also observed (see section VII of SM [43]).

3. Results and discussions

We begin by comparing the PW with the DFT training and assessment data to ensure that a good fit was achieved. For training data, the comparison is tabulated in table 3, except the third-order displacement IDs which are tabulated in table S2 of SM [43]. For the assessment data, the comparison for each property can be found by using table S1 of SM [43], including the second- and third-order displacement IDs in larger supercells, the formation energy for FPs in larger supercells, and thermal conductivity computed by using the BTE within the RTA. Overall, our parameter optimization process yields an EIP with relatively small errors relative to the DFT data. Interestingly, while the PW only has two training data points for the defect formation energy (i.e. FP of Th or U in a conventional cell of ThO_2 or UO_2, respectively), the PW can predict the formation energies for FPs of O, Th, and U in a larger supercell ($2 \times 2 \times 2$ of the conventional cell) reasonably well, all within 9% error compared with DFT (see table 4). For the sake of comparison, all of the aforementioned properties are also computed using the CRG.

We proceed to assess the PW via comparison with experiments and the CRG potential, which is fitted to experimental elastic constants and thermal expansion. For the phonon dispersion, figure 1 presents the comparison between DFT, EIPs, and experiments [35, 58, 59]. The CRG potential exhibits two deficiencies: the overprediction of all optical phonon branches and the inability to capture the phonon frequency gap between the highest two optical branches. As DFT can accurately capture the phonon dispersion in comparison with experiments, the PW, which is fitted to DFT, significantly improves the agreement of the optical phonon branches. Furthermore, a gap between the highest two optical branches is successfully predicted, which can be attributed to the core–shell model [41] (see section VII of SM [43] for more details). The only major deficiency of the PW for the phonon dispersion is the overprediction of the highest phonon mode near the X point. In the fitting procedure, the error of the highest phonon mode at the X point can be reduced by assigning a higher weight to that

Table 3. A portion of training data, including the second-order displacement IDs, the second-order strain IDs, lattice parameter at $T = 0$ (denoted $a(0)$), normalized Born effective charges Z^*_{Th} or Z^*_U, and the defect formation energy E_F for a Th or U FP in the conventional cubic supercell, computed by DFT, and compared with the CRG [7] and the PW.

	ThO_2			UO_2		
Property	SCAN	CRG	PW	PBE+U	CRG	PW
Second-order irreducible derivatives within the $2 \times 2 \times 2$ supercell (eV Å^{-2})						
$d^{T_{2g}T_{2g}}_{\Gamma\Gamma}$	12.65	16.02	12.82	11.64	17.35	12.90
$d^{T_{1u}T_{1u}}_{\Gamma\Gamma}$	12.75	16.60	11.62	10.91	15.63	10.06
$d^{A_{1g}A_{1g}}_{LL}$	17.47	16.28	16.87	16.11	17.34	17.67
$d^{E_gE_g}_{LL}$	9.57	11.10	9.14	8.69	11.64	9.01
$d^{A_{2u}A_{2u}}_{LL}$	35.76	32.75	34.01	30.50	32.04	28.83
$d^{A_{2u}{}^1A_{2u}}_{LL}$	7.78	6.69	5.73	6.63	7.72	4.14
$d^{{}^1A_{2u}{}^1A_{2u}}_{LL}$	10.07	16.10	9.97	8.72	17.14	8.36
$d^{E_uE_u}_{LL}$	9.59	12.22	9.62	7.93	11.25	8.15
$d^{E_u{}^1E_u}_{LL}$	−3.09	−6.57	−3.19	−2.62	−5.85	−2.49
$d^{{}^1E_u{}^1E_u}_{LL}$	7.55	11.10	7.47	6.89	11.64	6.75
$d^{A_{1g}A_{1g}}_{XX}$	21.02	27.18	25.23	19.74	29.87	26.53
$d^{E_gE_g}_{XX}$	4.61	4.11	3.03	3.70	3.55	2.57
$d^{{}^2A_{2u}{}^2A_{2u}}_{XX}$	41.53	28.64	31.60	37.25	28.23	26.95
$d^{B_{1u}B_{1u}}_{XX}$	2.53	2.86	1.91	1.55	2.10	1.39
$d^{E_uE_u}_{XX}$	12.09	19.62	12.79	11.38	21.45	11.68
$d^{E_u{}^1E_u}_{XX}$	−0.59	−4.12	−0.63	−0.24	−3.13	−0.23
$d^{{}^1E_u{}^1E_u}_{XX}$	11.79	14.76	13.67	9.40	13.33	11.69
Elastic energy irreducible strain derivatives (eV)						
$d_{A_{1g}A_{1g}}$	166.73	157.02	166.52	164.91	165.92	165.88
$d_{E_gE_g}$	70.81	64.78	68.89	69.48	71.25	66.55
$d_{T_{2g}T_{2g}}$	22.13	19.43	20.56	16.66	16.17	16.33
Other properties						
$a(0)$ (Å)	5.594	5.580	5.594	5.546	5.453	5.546
Z^*_{Th} or Z^*_U ($\|e\|$)	2.448	2.221	2.448	2.325	2.221	2.325
E_F(Th or U FP) (eV)	18.000	17.529	17.999	14.023	11.165	14.033

mode, but then all other phonon modes at the X point have a larger error, demonstrating the limitations of the potential form. Nevertheless, as the highest phonon branch has a negligible contribution to the thermal conductivity in ThO_2 and UO_2 [33, 36, 52], this error should not significantly affect the thermal transport (see section VI of SM [43] for more details). Table 4 tabulates the calculated elastic constants. Compared with experiments [60–62], the PW has better predictions than the CRG for C_{11} and C_{44} in ThO_2, and C_{44} in UO_2, though the CRG was directly fitted to experimental elastic constants. For the predictions of C_{12} in ThO_2 and C_{11} in UO_2, the PW is not as good as the CRG, but this is mainly due to the discrepancy between DFT and experiments. The thermal conductivity is computed and compared with experiments [63–69] in figure 2. The PW significantly improves the thermal conductivity prediction as compared to the CRG, which is expected, given that DFT has good agreement with experiments. For example, at $T = 1000$ K, the errors of predicted thermal conductivity by the CRG for ThO_2 and UO_2 are 54% and 63%, respectively, which are reduced to 17% and 9% by the PW, respectively, compared with experiments (see section VI of SM [43] for more details). Finally, we compare the thermal expansion predictions with experiments [66, 70]. As the CRG and the PW predict different $a(0)$, rather than comparing a directly, we compare the percentage change in lattice parameter, $\frac{a(T)-a(0)}{a(0)}$ (see in figure 3), with experiments. The PW gives good agreement with experiment up to $T = 2500$ K for both ThO_2 and UO_2, and slightly underpredicts the lattice parameter when $T > 2500$ K. In summary, the PW yields good agreement with the DFT data of IDs, $a(0)$, Z^*_α, the formation energy of FPs, and thermal conductivity. Compared with experiments, the PW also outperforms the CRG for phonon dispersions, elastic constants, and thermal

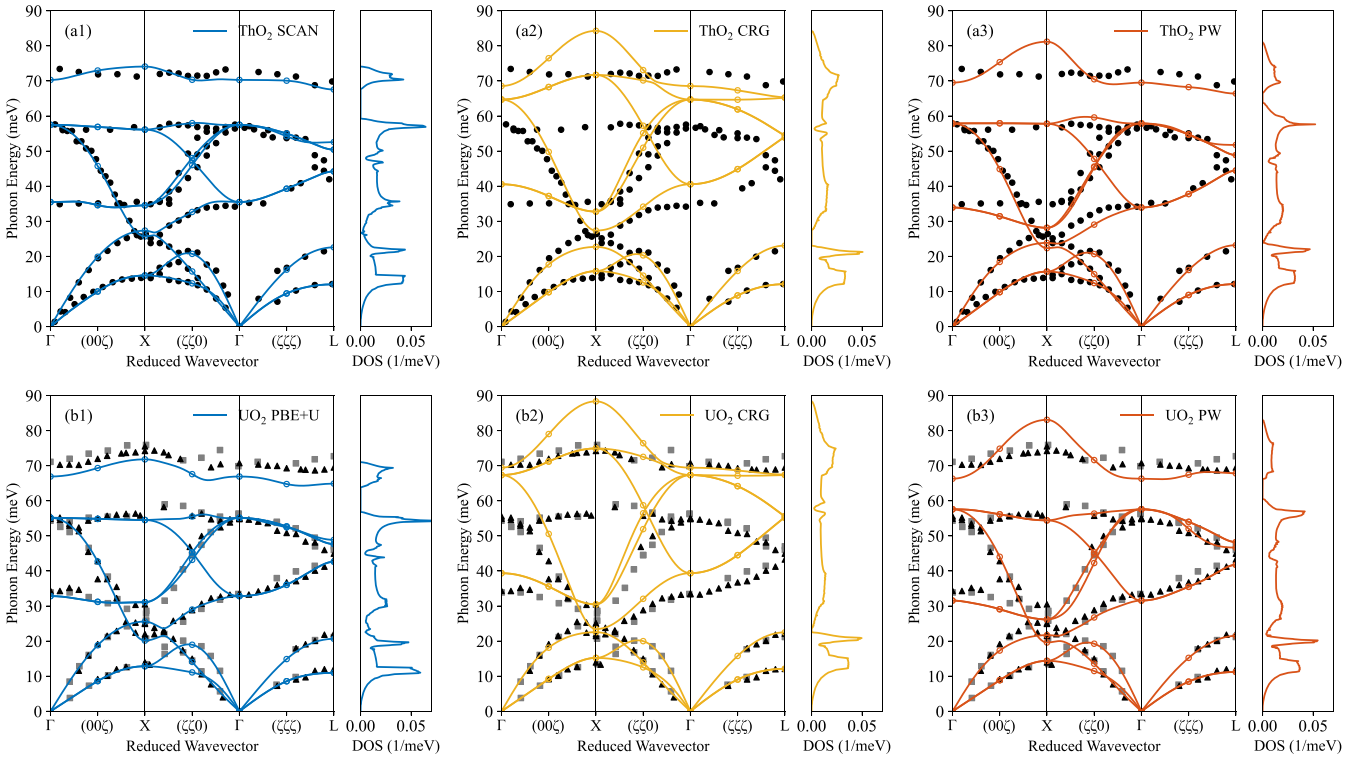

Figure 1. Calculated phonon dispersion and density of states for (a) ThO_2 and (b) UO_2, by using (1) DFT, (2) the CRG, and (3) the PW, compared to experimental data of ThO_2 (black circles) [58] and UO_2 (grey squares [59] and black triangles [36]). The lines are a Fourier interpolation of the computed data points, which are presented as open circles.

Table 4. Elastic constants and defect formation energy E_F for FPs calculated using DFT, the CRG, and the PW in comparison to experimental data [60–62]. See section IV of SM for definitions of FP1 and FP2 [43].

	ThO_2				UO_2			
Property	SCAN	CRG	PW	exp	PBE+U	CRG	PW	exp
				Elastic constants (GPa)				
C_{11}	376	352	371	367[a], 366[b]	380	406	374	400[c]
C_{12}	117	113	119	106[a], 114[b]	120	125	124	125[c]
C_{44}	81	72	75	80[a], 81[b]	63	64	61	59[c]
				Defect formation energy E_F (eV)				
O FP1	4.55	5.25	4.78		4.02	5.36	4.30	
O FP2	4.63	5.61	4.95		4.06	5.77	4.41	
Th or U FP	13.15	13.63	13.93		10.26	11.07	10.62	

[a] Macedo *et al* [60].
[b] Khanolkar *et al* [61].
[c] Brandt and Walker [62].

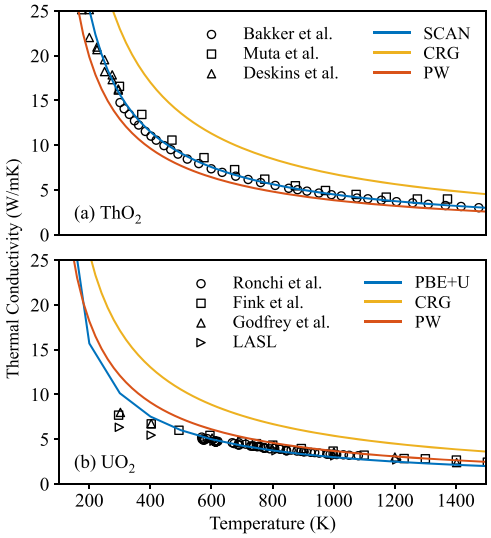

Figure 2. Calculated phonon thermal conductivity obtained from the BTE within the RTA for (a) ThO_2 and (b) UO_2, using DFT, the CRG, and the PW at $T = 100 - 1500$ K, compared with the experimental data of ThO_2 [63–65] and UO_2 [66–69].

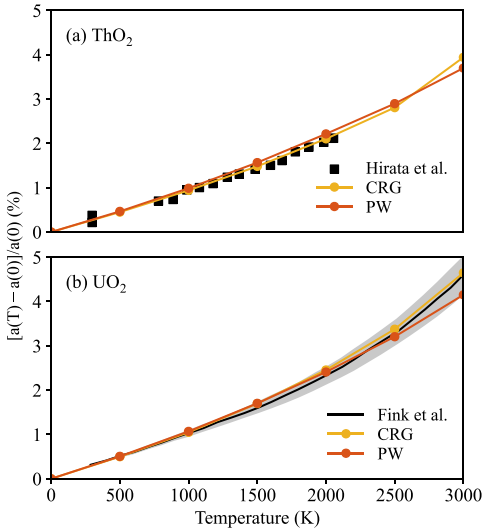

Figure 3. Calculated percentage change of the lattice parameter as a function of temperature at $T = 0 - 3000$ K obtained from molecular dynamics simulations for (a) ThO_2 and (b) UO_2 using the CRG and the PW, compared with the experimental data of ThO_2 [70] and UO_2 [66].

conductivity, except for certain elastic constants where DFT has discrepancies with experiments, and thermal expansion at high temperatures where there is likely insufficient training data.

4. Conclusion

In this work, we developed an interatomic potential training approach by utilizing IDs, including second- and third-order displacement IDs and second-order strain IDs, calculated from DFT. This ID-based potential training approach was used to construct an EIP for ThO_2 and UO_2 crystals, yielding an EIP with relatively small errors relative to the DFT data, including the aforementioned IDs, phonon dispersion, thermal conductivity, and the formation energy of FPs. Compared with experiments, the PW outperforms the widely used CRG potential [7] for phonon dispersions and thermal conductivity. In addition to using a far more expansive training data set for our EIP, we also enhanced the analytical functional form for our EIP to include a core–shell model, which was essential for capturing selected optical phonon modes. Our ID-based framework can straightforwardly be applied to more complex systems, such as random alloys, where the main limitation is mainly associated with the computational cost of computing the IDs using DFT, rather than the model training procedure. Training EIPs based on IDs is clearly a promising direction for developing accurate interatomic potentials focused on predicting phonon-related thermophysical properties, and this approach will likely be useful in the broader context of machine learning-based potentials.

Data availability statement

All data that support the findings of this study are included within the article (and any supplementary files).

Acknowledgments

This work was supported by the Center for Thermal Energy Transport under Irradiation, an Energy Frontier Research Center funded by the U.S. Department of Energy (DOE) Office of Basic Energy Sciences. This research made use of the resources of the High Performance Computing Center at Idaho National Laboratory, which is supported by the Office of Nuclear Energy of the U.S. Department of Energy and the Nuclear Science User Facilities under Contract No. DE-AC07-05ID14517. M W D C acknowledges support from the Nuclear Energy Advanced Modeling and Simulation (NEAMS) Program funded by the U.S. DOE Office of Nuclear Energy. S B, E X, and C A M acknowledge resources of the National Energy Research Scientific Computing Center, a DOE Office of Science User Facility supported by the Office of Science of the U.S. Department of Energy under Contract No. DE-AC02-05CH11231. Grant DE-SC0016507 supported S B and C A M for integrating empirical potentials in the irreducible derivative framework.

ORCID iDs

Shuxiang Zhou https://orcid.org/0000-0002-5029-1251
Miaomiao Jin https://orcid.org/0000-0002-3543-4082
Marat Khafizov https://orcid.org/0000-0001-8171-3528
Chris A Marianetti https://orcid.org/0000-0003-3812-2751

References

[1] Lennard–Jones J E 1931 *Proc. Phys. Soc.* **43** 461
[2] Tersoff J 1988 *Phys. Rev. B* **38** 9902

[3] Daw M S and Baskes M I 1984 *Phys. Rev. B* **29** 6443
[4] Behler J and Parrinello M 2007 *Phys. Rev. Lett.* **98** 146401
[5] Bartók A P, Payne M C, Kondor R and Csányi G 2010 *Phys. Rev. Lett.* **104** 136403
[6] Allen M P and Tildesley D J 2017 *Computer Simulation of Liquids* 2nd edn (Clarendon)
[7] Cooper M W D, Rushton M J D and Grimes R W 2014 *J. Phys.: Condens. Matter* **26** 105401
[8] Chernatynskiy A, Flint C, Sinnott S and Phillpot S 2012 *J. Mater. Sci.* **47** 7693
[9] Ercolessi F and Adams J B 1994 *Europhys. Lett.* **26** 583
[10] Mishin Y, Farkas D, Mehl M and Papaconstantopoulos D 1999 *Phys. Rev. B* **59** 3393
[11] Fellinger M R, Park H and Wilkins J W 2010 *Phys. Rev. B* **81** 144119
[12] Lee Y and Hwang G S 2012 *Phys. Rev. B* **85** 125204
[13] Brommer P, Kiselev A, Schopf D, Beck P, Roth J and Trebin H-R 2015 *Modelling Simul. Mater. Sci. Eng.* **23** 074002
[14] Schopf D, Euchner H and Trebin H-R 2014 *Phys. Rev. B* **89** 214306
[15] Roy Chowdhury P, Feng T and Ruan X 2019 *Phys. Rev. B* **99** 155202
[16] Cooper M W D, Kuganathan N, Burr P A, Rushton M J D, Grimes R W, Stanek C R and Andersson D A 2016 *J. Phys.: Condens. Matter* **28** 405401
[17] Novikov I S, Gubaev K, Podryabinkin E V and Shapeev A V 2020 *Mach. Learn.: Sci. Technol.* **2** 025002
[18] Chahal R, Roy S, Brehm M, Banerjee S, Bryantsev V and Lam S T 2022 *JACS Au* **2** 2693
[19] Attarian S, Morgan D and Szlufarska I 2024 *J. Mol. Liq.* **400** 124521
[20] Lindsay L and Broido D 2010 *Phys. Rev. B* **81** 205441
[21] Murakami T, Shiga T, Hori T, Esfarjani K and Shiomi J 2013 *Europhys. Lett.* **102** 46002
[22] Han P and Bester G 2011 *Phys. Rev. B* **83** 174304
[23] Muraleedharan M G, Rohskopf A, Yang V and Henry A 2017 *AIP Adv.* **7** 125022
[24] Rohskopf A, Wyant S, Gordiz K, Seyf H R, Muraleedharan M G and Henry A 2020 *Comput. Mater. Sci.* **184** 109884
[25] Shi L, Ma X, Li M, Zhong Y, Yang L, Yin W and He X 2021 *Phys. Chem. Chem. Phys.* **23** 8336
[26] Loew A, Wang H-C, Cerqueira T F and Marques M A 2024 *Mach. Learn.: Sci. Technol.* **5** 045019
[27] Fang S, Geiger M, Checkelsky J G and Smidt T 2024 Phonon predictions with E(3)-equivariant graph neural networks (arXiv:2403.11347 [cond-mat])
[28] Fu L, Kornbluth M, Cheng Z and Marianetti C A 2019 *Phys. Rev. B* **100** 014303
[29] Hurley D H *et al* 2022 *Chem. Rev.* **122** 3711
[30] Park J, Farfán E B, Mitchell K, Resnick A, Enriquez C and Yee T 2018 *J. Nucl. Mater.* **504** 198
[31] Balboa H, Van Brutzel L, Chartier A and Le Bouar Y 2017 *J. Nucl. Mater.* **495** 67
[32] Malakkal L, Prasad A, Jossou E, Ranasinghe J, Szpunar B, Bichler L and Szpunar J 2019 *J. Alloys Compd.* **798** 507
[33] Jin M, Khafizov M, Jiang C, Zhou S, Marianetti C A, Bryan M S, Manley M E and Hurley D H 2021 *J. Phys.: Condens. Matter* **33** 275402
[34] Dennett C A *et al* 2021 *Acta Mater.* **213** 116934
[35] Zhou S, Ma H, Xiao E, Gofryk K, Jiang C, Manley M E, Hurley D H and Marianetti C A 2022 *Phys. Rev. B* **106** 125134
[36] Zhou S, Xiao E, Ma H, Gofryk K, Jiang C, Manley M E, Hurley D H and Marianetti C A 2024 *Phys. Rev. Lett.* **132** 106502
[37] Buckingham R A and Lennard–Jones J E 1938 *Proc. R. Soc. A* **168** 264
[38] Morse P M 1929 *Phys. Rev.* **34** 57
[39] Mitchell P J and Fincham D 1993 *J. Phys.: Condens. Matter* **5** 1031
[40] Govers K, Lemehov S, Hou M and Verwerft M 2007 *J. Nucl. Mater.* **366** 161
[41] Thompson A E, Meredig B, Stan M and Wolverton C 2014 *J. Nucl. Mater.* **446** 155
[42] Gale J D 1997 *J. Chem. Soc. Faraday Trans.* **93** 629
[43] See supplemental material online for details of the training and assessment data, the training method for empirical potential, the training results for alternative analytical forms, the configurations of Frenkel pairs, the analyses and comparisons of second- and third-order irreducible derivatives, and the reciprocal coordinates of primary q points and their displacement bases. See also [71].
[44] Blöchl P E 1994 *Phys. Rev. B* **50** 17953
[45] Kresse G and Joubert D 1999 *Phys. Rev. B* **59** 1758
[46] Kresse G and Hafner J 1993 *Phys. Rev. B* **47** 558
[47] Kresse G and Furthmüller J 1996 *Phys. Rev. B* **54** 11169
[48] Sun J, Ruzsinszky A and Perdew J P 2015 *Phys. Rev. Lett.* **115** 036402
[49] Perdew J P, Burke K and Ernzerhof M 1996 *Phys. Rev. Lett.* **77** 3865
[50] Maldonado P, Paolasini L, Oppeneer P, Forrest T R, Prodi A, Magnani N, Bosak A, Lander G and Caciuffo R 2016 *Phys. Rev. B* **93** 144301
[51] Mathis M A *et al* 2022 *Phys. Rev. B* **106** 014314
[52] Xiao E *et al* 2022 *Phys. Rev. B* **106** 144310
[53] Anisimov V I, Zaanen J and Andersen O K 1991 *Phys. Rev. B* **44** 943
[54] Dudarev S L, Manh D N and Sutton A P 1997 *Phil. Mag. B* **75** 613
[55] Monkhorst H J and Pack J D 1976 *Phys. Rev. B* **13** 5188
[56] Ewald P P 1921 *Ann. Phys., Lpz.* **369** 253
[57] Rushton M J 2023 potential-pro-fit (available at: https://github.com/mjdrushton/potential-pro-fit) (Accessed 9 June 2025)
[58] Bryan M S, Pang J W L, Larson B C, Chernatynskiy A, Abernathy D L, Gofryk K and Manley M E 2019 *Phys. Rev. Mater.* **3** 065405
[59] Pang J W L, Buyers W J L, Chernatynskiy A, Lumsden M D, Larson B C and Phillpot S R 2013 *Phys. Rev. Lett.* **110** 157401
[60] Macedo P M, Capps W and Wachtman J O 1964 *J. Am. Ceram. Soc.* **47** 651
[61] Khanolkar A, Wang Y, Dennett C A, Hua Z, Mann J M, Khafizov M and Hurley D H 2023 *J. Appl. Phys.* **133** 195101
[62] Brandt O G and Walker C T 1967 *Phys. Rev. Lett.* **18** 11
[63] Deskins W R *et al* 2022 *Acta Mater.* **241** 118379
[64] Muta H, Murakami Y, Uno M, Kurosaki K and Yamanaka S 2013 *J. Nucl. Sci. Technol.* **50** 181
[65] Bakker K, Cordfunke E H P, Konings R J M and Schram R P C 1997 *J. Nucl. Mater.* **250** 1
[66] Fink J K 2000 *J. Nucl. Mater.* **279** 1
[67] Bates J L 1965 *Nucl. Sci. Eng.* **21** 26
[68] Godfrey T G, Fulkerson W, Kollie T G, Moore J P and McElroy D L 1965 *J. Am. Ceram. Soc.* **48** 297
[69] Ronchi C, Sheindlin M, Staicu D and Kinoshita M 2004 *J. Nucl. Mater.* **327** 58
[70] Hirata K, Moriya K and Waseda Y 1977 *J. Mater. Sci.* **12** 838
[71] Momma K and Izumi F 2011 *J. Appl. Crystallogr.* **44** 1272